

Accepted by the Astrophysical Journal 15 Dec 2010

# Achieving Self-Consistent Nonlinear Force-free Modeling of Solar Active Regions

M. S. Wheatland

*Sydney Institute for Astronomy, School of Physics, The University of Sydney, NSW 2006, Australia*

michael.wheatland@sydney.edu.au

and

K. D. Leka

*North West Research Associates, Colorado Research Associates Division, 3380 Mitchell Lane, Boulder, CO 80301, USA*

leka@cora.nwra.com

## ABSTRACT

A nonlinear force-free solution is constructed for the coronal magnetic field in NOAA solar active region AR 10953 based on a photospheric vector magnetogram derived from Hinode satellite observations on 30 April 2007, taking into account uncertainties in the boundary data and using improved methods for merging multiple-instrument data. The solution demonstrates the ‘self-consistency’ procedure of Wheatland & Régnier (2009), for the first time including uncertainties. The self-consistency procedure addresses the problem that photospheric vector magnetogram data are inconsistent with the force-free model, and in particular that the boundary conditions on vertical electric current density are over-specified and permit the construction of two different nonlinear force-free solutions. The procedure modifies the boundary conditions on current density during a sequence of cycles until the two nonlinear force-free solutions agree. It hence constructs an accurate single solution to the force-free model, with boundary values close, but not matched exactly, to the vector magnetogram data. The inclusion of uncertainties preserves the boundary conditions more closely at points with smaller uncertainties. The self-consistent solution obtained for active region AR 10953 is

significantly non-potential, with magnetic energy  $E/E_0 \approx 1.08$ , where  $E_0$  is the energy of the reference potential (current-free) magnetic field. The self-consistent solution is shown to be robust against changes in the details of the construction of the two force-free models at each cycle. This suggests that reliable nonlinear force-free modeling of active regions is possible if uncertainties in vector magnetogram boundary data are included.

*Subject headings:* Sun: corona — Sun: magnetic fields

## 1. Introduction

Intense magnetic fields around sunspot regions drive the most energetic examples of solar activity – large solar flares and coronal mass ejections – which can produce hazardous space weather conditions close to Earth. Severe space weather storms present a variety of hazards including increased radiation levels for space travellers and crew on polar air flights, the risks of disabling of GPS systems and damage to power grids (Committee On The Societal & Economic Impacts 2008), and potential large economic losses due to damage to communications satellites (Odenwald et al. 2006). These effects motivate a need to understand and model the source regions of space weather threats at the Sun.

Spectro-polarimetric measurements of magnetically sensitive photospheric lines may be used to infer the vector magnetic field at the surface of the Sun (Landi Degl’Innocenti & Landolfi 2004), and the resulting maps of the field are called vector magnetograms. A new generation of instrumentation is set to provide vector magnetogram data over the next solar cycle with unprecedented quality, resolution, and temporal cadence, including the Solar Optical Telescope Spectro-Polarimeter (SOT/SP) on the Hinode spacecraft (Tsuneta et al. 2008) and the Helioseismic and Magnetic Imager on the Solar Dynamics Observatory (SDO/HMI) (Scherrer, Hoeksema, & the HMI Team 2006; Borrero et al. 2007). In principle these measurements provide boundary values for coronal magnetic field modeling, or ‘magnetic field reconstruction’. There is a pressing need for this modeling capability, which has many potential applications in solar research. However, studies have revealed basic difficulties preventing the construction of reliable coronal field models from vector magnetograms using present modeling techniques. Specifically, a popular and well-developed approach to magnetic field reconstruction, nonlinear force-free modeling, has been shown to produce inconsistent results when applied to Hinode/SOT vector magnetogram data (Schrijver et al. 2008; De Rosa et al. 2009; Wheatland et al. 2010). Different modeling codes produce different results based on the same data, and the results from individual codes are also internally inconsistent. As described in more detail in section 2, vector magnetograms allow for two

sets of boundary conditions for the force-free model, and the two solutions do not in general agree. It is also difficult to construct the solutions: the boundary conditions on electric current present large currents which prevent the force-free methods from converging strictly. As a result the ‘solutions’ may be inaccurate with respect to the model. The modeling has been shown to be unable to provide a reliable estimate of the free magnetic energy of a solar active region. Further details of the problems are provided in section 2.

One likely cause of the failure of nonlinear force-free modeling is a basic inconsistency between the boundary data and the model: the model includes only magnetic forces, an assumption that may be warranted in the corona, but which is thought not to apply at the photospheric level where the data originate (Metcalf et al. 1995). Recently a new approach to coronal magnetic field reconstruction was presented to address this problem (Wheatland & Régnier 2009). The ‘self-consistency’ procedure (described in more detail in section 2) identifies a nonlinear force-free solution with boundary values close to those implied by the vector magnetogram data. The method constructs a single solution to the nonlinear force-free model which strictly converges. The solution does not match exactly the field at the photospheric level, but may describe the coronal magnetic field. In Wheatland & Régnier (2009) the method was demonstrated in application to Hinode/SOT data for NOAA active region 10953. A solution to the model was constructed with energy  $E/E_0 \approx 1.02$ , where  $E_0$  is the energy of the reference potential (current-free) magnetic field matching the boundary conditions on the vertical component of the field. The self-consistency procedure is capable of taking into account relative uncertainties in the solar boundary data, so that the boundary values for the solution match the vector magnetogram data more closely at points with small uncertainties. However, uncertainties were omitted from the Wheatland & Régnier (2009) calculations, and this omission accounts in part for the low value of the magnetic free energy of the constructed solution (2% of the energy of the potential field), as explained in section 2.4. For this reason the results in Wheatland & Régnier (2009) were argued to represent a ‘proof in concept’ of the self-consistency procedure, rather than a full demonstration of its modeling capability. In this paper we return to the problem of modeling AR 10953, including uncertainties in the calculation.

The detailed presentation of this paper is as follows. Section 2 provides a more detailed account of the background to the modeling presented here, including a summary of the nonlinear force-free model (section 2.1), a description of the failure of the model in application to solar data (section 2.2), and an account of the self-consistency procedure (section 2.3) and its initial application to AR 10953 by Wheatland & Régnier (2009) (section 2.4). A reader familiar with the background may skim or omit section 2, but it provides necessary background for a reader new to the topic. Section 3 describes the modeling of AR 10953 taking into account uncertainties, with section 3.1 presenting the data, and section 3.2 the

results of the modeling. Section 4 discusses the results.

## 2. Background

### 2.1. Nonlinear force-free model

Magnetic fields in the corona are often described as being force free (Sturrock 1994). The force-free model is static and includes only the magnetic (Lorentz) force, an approximation justified by the low ratio of gas pressure to magnetic pressure likely to exist at most locations in the corona (Metcalf et al. 1995; Gary 2001). A force-free magnetic field  $\mathbf{B}$  satisfies

$$\mathbf{B} \cdot \nabla \alpha = 0 \quad \text{and} \quad \nabla \times \mathbf{B} = \alpha \mathbf{B}, \quad (1)$$

where  $\alpha$  is the force-free parameter. This parameter is constant along field lines, but varies (in general) from field line to field line, and the implicit dependence of  $\alpha$  on  $\mathbf{B}$  makes the model nonlinear. The boundary conditions required by the model are the normal component of  $\mathbf{B}$  in the boundary (denoted  $B_n$ ), and a specification of  $\alpha$  over one polarity (sign) of  $B_n$  (e.g. Grad & Rubin 1958; Sakurai 1981; Aly 1989; Amari et al. 2006). We denote the two polarities  $P$  (positive) and  $N$  (negative), for boundary points with  $B_n > 0$  and  $B_n < 0$  respectively (assuming a normal directed into the coronal volume). The boundary condition on  $\alpha$  is equivalent to a specification of the normal component of the electric current density  $\mathbf{J}$  over either  $P$  or  $N$ , because  $\mathbf{J} = \alpha \mathbf{B} / \mu_0$  in the model.

A number of numerical methods of solution of the nonlinear force-free equations have been developed in the solar context [for recent reviews see e.g. Neukirch (2005); Aly & Amari (2007); Régnier (2007); Wiegelmann (2008)]. Most methods focus on the solution of the problem in a half space ( $z > 0$ ), with the lower boundary ( $z = 0$ ) representing the photosphere, solar curvature being neglected. The different methods vary in terms of numerical methods and in the treatment of boundary conditions. Some methods – e.g. the optimization method (Wheatland et al. 2000; Wiegelmann 2004) – use the full vector magnetic field over both  $P$  and  $N$  in the lower boundary as a boundary condition. This is formally an over-prescription, but does not introduce a problem provided the boundary conditions are consistent with the model, as shown by application to test cases (Schrijver et al. 2006). Methods based on the ‘current-field iteration’ or Grad-Rubin procedure (Grad & Rubin 1958; Sakurai 1981; Amari et al. 1997, 2006) use the formally correct boundary conditions on  $\alpha$  described above. A Grad-Rubin implementation is the basis for the calculations in this paper (Wheatland 2007). These methods work by replacing the nonlinear force-free equations by a sequence of iterations, such that at the  $i^{\text{th}}$  iteration the linear equations

$$\mathbf{B}^{[i-1]} \cdot \nabla \alpha^{[i]} = 0 \quad \text{and} \quad \nabla \times \mathbf{B}^{[i]} = \alpha^{[i]} \mathbf{B}^{[i-1]}, \quad (2)$$

are solved for  $\mathbf{B}^{[i]}$  given  $\mathbf{B}^{[i-1]}$ , subject to  $\nabla \cdot \mathbf{B}^{[i]} = 0$  and the boundary conditions on  $\alpha^{[i]}$  and  $\mathbf{B}^{[i]}$ . For the half space problem the boundary conditions are the specification of  $B_z^{[i]}$  at  $z = 0$  and  $\alpha^{[i]}$  at  $z = 0$  over either  $P$  or  $N$ . The iteration is usually started by setting  $\mathbf{B}^{[0]}$  equal to the reference potential (current-free) field matching the boundary conditions on  $B_z$ . A fixed point of the iteration scheme specified by Equations (2) provides a solution to the nonlinear force-free Equations (1).

## 2.2. Failure of nonlinear force-free modeling for solar data

Although the nonlinear force-free methods work well in application to test cases (Schrijver et al. 2006) and to synthetic solar-like data (Metcalf et al. 2008), the application to vector magnetogram data has revealed serious problems. Tests of different methods using Hinode/SOT data for NOAA active regions AR 10930 (Schrijver et al. 2008) and AR 10953 (De Rosa et al. 2009) produced very different solutions for each active region depending on the specific method used. In particular the estimated magnetic free energy of each active region varied substantially among the solutions, preventing reliable determination of this quantity. Perhaps worse, the solutions from particular methods were also found to be internally inconsistent. For example, for the Grad-Rubin methods the vector magnetogram data provide both the  $P$  and  $N$  choices for the boundary conditions on the force-free parameter. Specifically,  $\alpha$  may be estimated from the data at the photosphere ( $z = 0$ ) by calculating the gradients in the observationally-inferred transverse fields  $B_x$  and  $B_y$  according to

$$\alpha = \frac{1}{B_z} \left( \frac{\partial B_y}{\partial x} - \frac{\partial B_x}{\partial y} \right), \quad (3)$$

and these values are available over both  $P$  and  $N$ . The  $P$  and  $N$  solutions obtained by applying the Wheatland (2007) current-field iteration method to the data for active regions AR 10930 and AR 10953 were found to be very different (Schrijver et al. 2008; De Rosa et al. 2009).

It is likely that a number of factors contribute to the failure of the modeling. Vector magnetogram field values are approximate due to resolution limitations, modeling assumptions, and photon noise in the polarization measurements. Assumptions made in the inference of the field from the Stokes spectral measurements (Del Toro Iniesta & Ruiz Cobo 1996; Landi Degl’Innocenti & Landolfi 2004), for example using a Milne-Eddington atmosphere, introduce inaccuracy (Auer et al. 1977; Skumanich & Lites 1987; Bommier et al. 2007). The values are also uncertain due to the influence of instrumental noise and resolution limitations on the polarization measurements. The component of the magnetic field transverse to the line of sight is particularly uncertain due to the intrinsically smaller linear polarization signal

relative to the integrated intensity, magneto-optical effects (Landolfi & Landi Degl’Innocenti 1982), and the need to resolve an intrinsic 180-degree ambiguity in the azimuthal direction of the field (Metcalf 1994; Metcalf et al. 2006; Leka et al. 2009).

A problem with the force-free modeling is that different methods of solving the Equations (1) make different assumptions regarding the problem of the ‘missing’ boundary conditions at the sides and top boundaries of the computational domain. These different assumptions lead (not surprisingly) to different results (Schrijver et al. 2006; Metcalf et al. 2008; Schrijver et al. 2008; De Rosa et al. 2009). However, the modeling also faces a more fundamental difficulty: the magnetic field at the height of the measurements is unlikely to be force free because the dense photospheric gas is subject to pressure, gravity, and dynamical forces in addition to the magnetic forces (Metcalf et al. 1995). The boundary data are fundamentally inconsistent with the model.

The accuracy of the force-free assumption for the boundary data may be checked a priori by calculating integrals of the field in the boundary representing the net magnetic flux, the net force and the torque on the field in  $z > 0$  (Molodenskii 1969; Aly 1984, 1989). The requirement that these integrals vanish provides a set of necessary conditions for the existence of a force-free solution for given boundary data. In general the integrals are found to be substantially different from zero for photospheric vector magnetogram data. One treatment of this problem is a procedure called ‘preprocessing,’ whereby the boundary data are varied to minimize the integrals, subject to constraints (Wiegelmann, Inhester, & Sakurai 2006; Wiegelmann et al. 2008). Preprocessing has been found to improve nonlinear force-free reconstructions from synthetic solar data for some methods (Metcalf et al. 2008), and preprocessed data were used in the modeling of active regions AR 10930 and AR 10953 presented by Schrijver et al. (2008) and De Rosa et al. (2009) respectively. However, there are non-trivial problems with the preprocessing approach. First, the conditions being minimized are necessary but not sufficient, so there is an arbitrary number of such constraints (Aly 1989; Régnier 2007). The minimization procedure will not satisfy all such constraints, and it is straightforward to show that preprocessed boundary data are still inconsistent with the force-free model (De Rosa et al. 2009). As a result, the  $P$  and  $N$  solutions constructed by Grad-Rubin methods still disagree, and ‘force-free solutions’ constructed using other methods, e.g. the optimization method (Wheatland et al. 2000; Wiegelmann 2004) must be internally inconsistent with the force-free model. The situation is then that the observed boundary data is not matched by the ‘solution,’ and the force-free model is not being accurately solved. A second problem is that preprocessing typically involves a smoothing of the data, which is undesirable because it discards information. Recently, another solution was proposed, in which a vector field is calculated which attempts to simultaneously minimize the Lorentz force, the divergence, and the departure from observed boundary conditions, using

an optimization-like procedure (Wiegelmann & Inhester 2010). However, this method also fails to adhere to the force-free equations or retain (to within measurement uncertainties) the observed boundary data.

A related problem with solar nonlinear force-free modeling is that the boundary conditions on the vertical electric current density  $J_z$  corresponding to vector-magnetogram derived values of  $\alpha$  include very large electric currents. The values of the current density are considerably uncertain because of the uncertainties in the field determinations discussed above, and there is also dependence of the values on the observational spatial resolution, which changes when field values are interpolated onto new grids and rebinned (Leka 1999; Leka et al. 2009). Nevertheless there appear to be electric currents sufficiently large to be inconsistent with the force-free model, which prevent strict convergence of nonlinear force-free methods (Schrijver et al. 2008; De Rosa et al. 2009). The Wheatland (2007) method is often found to reach a state where the field configuration exhibits slow oscillation as a function of Grad-Rubin iteration number rather than achieving a fixed state. The energy of the solution also oscillates slowly as a function of iteration number. This behavior suggests the non-existence, or the non-uniqueness, of a solution to the boundary value problem being solved (Amari et al. 2006; Inhester & Wiegelmann 2006). The consequence of this problem for the modeling is that the solution is non-unique (the exact result depends on the arbitrary choice of a stopping iteration) and also the force-free model is being solved less accurately (the field is less force free than in the case of strict convergence because the Grad-Rubin procedure does not achieve a fixed point).

### 2.3. Self-consistency procedure

In this paper we adopt the approach to resolving the inconsistency problem introduced recently by Wheatland & Régnier (2009). The ‘self-consistency’ procedure identifies one nonlinear force-free solution with boundary values close, but not exactly matched, to the vector magnetogram data, with guidance from the estimated uncertainties. The result is an accurate solution within the assumptions of the force-free model. The procedure may be summarized as follows.

First,  $P$  and  $N$  nonlinear force-free solutions are constructed, from unprocessed vector magnetogram boundary data, using the Grad-Rubin code of Wheatland (2007), with a chosen number of iterations. These solutions use boundary values  $\alpha_0 \pm \sigma_0$  for the force-free parameter, where the  $\alpha_0$  values are derived from the vector magnetogram data via Equation (3), and the uncertainties  $\sigma_0$  are obtained by propagating the uncertainties assigned to the field values (Leka & Skumanich 1999). The  $P$  solution provides a mapping, along field

lines, of the observational boundary values  $\alpha_0 \pm \sigma_0$  at points in the region  $P$  to points in  $N$ . This defines new possible boundary values  $\alpha_1 \pm \sigma_1$  of the force-free parameter at points in  $N$ . (These values will not match the observational values  $\alpha_0 \pm \sigma_0$  due to the inconsistency problem.) Similarly, the  $N$  solution maps the observational boundary values  $\alpha_0 \pm \sigma_0$  at points  $N$  to points in  $P$ , and so defines new possible boundary values  $\alpha_1 \pm \sigma_1$  at points in  $P$ . Together the two solutions define a complete new set of boundary values  $\alpha_1 \pm \sigma_1$  of the force-free parameter (over  $P$  and  $N$ ). Figure 1 illustrates the first step of the self-consistency procedure.

Second, Bayesian probability theory (Jaynes 2003) is applied to decide on a boundary value of the force-free parameter at each boundary point, based on the two sets of values  $\alpha_0 \pm \sigma_0$  and  $\alpha_1 \pm \sigma_1$ . The idea is that the values represent two observations subject to Gaussian uncertainties, and Bayes’s theorem is applied to determine the true value of the force-free parameter. The resulting most probable value and associated uncertainty are given by the uncertainty-weighted averages (Wheatland & Régnier 2009):

$$\alpha_2 = \frac{\alpha_0/\sigma_0^2 + \alpha_1/\sigma_1^2}{1/\sigma_0^2 + 1/\sigma_1^2} \quad \text{and} \quad \sigma_2 = \left( \frac{1}{\sigma_0^2} + \frac{1}{\sigma_1^2} \right)^{-1/2}. \quad (4)$$

The resulting set of boundary values  $\alpha_2 \pm \sigma_2$  over  $P$  and  $N$  is still, in general, inconsistent with the force-free model, but the values are expected to be closer to consistency.

Finally, steps one and two are iterated. Two force-free solutions (the  $P$  and  $N$  solutions) are constructed from the new boundary values  $\alpha_2 \pm \sigma_2$ , again by applying current-field iteration, in each case. The two solutions define new mappings between the  $P$  and  $N$  regions, and hence a complete new set of boundary conditions  $\alpha_3 \pm \sigma_3$ . Equations (4) are applied to the two sets of values  $\alpha_2 \pm \sigma_2$  and  $\alpha_3 \pm \sigma_3$  to decide on most probable values  $\alpha_4 \pm \sigma_4$  at each boundary point, and so on. Each iteration of the self-consistency procedure [i.e. the construction of the  $P$  and  $N$  solutions, and then the application of Equations (4) to give a new set of boundary conditions on current] is referred to as a ‘self-consistency cycle.’ The cycles are numbered starting at one, and the  $P$  and  $N$  solutions are enumerated with an index  $k$ , such that the first cycle involves construction of  $P$  and  $N$  solutions for the vector magnetogram boundary values  $\alpha_0 \pm \sigma_0$ , with the solutions numbered  $k = 1$  and  $k = 2$  respectively.

Self-consistency cycling is expected to converge to a self-consistent solution, i.e. a set of boundary values of the force-free parameter for which the  $P$  and  $N$  solutions are the same. The result is a single force-free solution, with (in some sense) a minimal departure from the observations.



## 2.4. Wheatland & Régnier (2009)

In Wheatland & Régnier (2009) the self-consistency procedure was demonstrated in application to Hinode/SOT data for AR 10953 observed at 22:30 UT on 30 April 2007. The vector magnetogram was the same as that described in De Rosa et al. (2009) but without the preprocessing (and associated smoothing). Uncertainties were assumed to be equal at each boundary point. In that case the first of Equations (4) reduces to  $\alpha_2 = \frac{1}{2}(\alpha_0 + \alpha_1)$ , i.e. a simple average of the two values. The self-consistency procedure was applied for ten cycles and found to converge to a solution with an energy  $E/E_0 \approx 1.02$ , where  $E_0$  is the energy of the reference potential field.

Figure 2 illustrates the self-consistent solution obtained by Wheatland & Régnier (2009). Panel (a) shows the  $P$  solution and panel (b) shows the  $N$  solution, after 10 self-consistency cycles. Each image looks down on the central part of the computational volume. The red-white-blue image in the background shows the boundary values of  $B_z$ , with red indicating negative values, white values close to zero, and blue positive values. Two sets of field lines are shown in each panel by the red and the blue curves. The blue curves are field lines originating at points in the  $P$  polarity and the red curves are field lines originating at points in the  $N$  polarity. The sets of field lines in panel (a) and in panel (b) agree closely, illustrating the achievement of self-consistency. Figure 1 in Wheatland & Régnier (2009) (not reproduced here) also shows the  $P$  and  $N$  solutions at the first self-consistency cycle, i.e. calculated directly from the original boundary data. The initial  $P$  and  $N$  solutions disagree markedly, with the  $N$  solution having more highly distorted magnetic field lines than the  $P$  solution, due to large electric currents associated with the leading polarity negative spot in the region.

The self-consistent solution shown in Figure 2 has a relatively small magnetic free energy (about 2% of the energy of  $E_0$ ). As discussed in Wheatland & Régnier (2009), this is due in part to the neglect of uncertainties in the boundary values of  $\alpha$ . Many of the boundary points have zero values of  $\alpha$ . The Hinode field of view is small, and to compensate for this the Hinode data was embedded in a larger field of view based on a line-of-sight magnetogram from the Michelson Doppler Interferometer (MDI) instrument on the Solar and Heliospheric Observatory (SOHO) spacecraft (Scherrer et al. 1995). The SOHO/MDI data points have zero values for  $J_z$  and hence for  $\alpha$ , and these zero boundary values are given equal weight to non-zero Hinode-derived values of  $\alpha$  in the self-consistency averaging of the first of Equations (4). This leads to a reduction in the electric currents in the solution, and hence a reduction in the magnetic free energy. Also, some strong currents are expected to occur in strong field regions, which will have more accurately-determined field values in the vector magnetograms (smaller uncertainties). These larger currents would be preserved in the ap-

plication of Equations (4) with uncertainties included. This is expected also to contribute to a reduction in the currents in the Wheatland & Régnier (2009) solution. For these reasons the solution was presented as a proof of concept of the self-consistency procedure, rather than as a realistic attempt to model AR 10953.

### 3. Modeling of AR 10953 including uncertainties

#### 3.1. Data

The calculations presented here use a set of data for NOAA AR 10953 derived from the same Hinode/SOT SpectroPolarimeter (Tsuneta et al. 2008) observations at 22:30 UT on 30 April 2007 previously used in De Rosa et al. (2009) and Wheatland & Régnier (2009). The original Hinode data are again inverted with the HAO/ASP inversion code developed by Paul Seagraves at NCAR/HAO (B. W. Lites 2009) which was used previously. The code provides estimates of the uncertainties in each magnetic component derived from the  $\chi^2$  variation of the least-squares fit results for the observed Stokes spectra. These error estimates may be considered to provide a lower limit for the uncertainty in any single measurement. Standard error propagation is applied to the transformations used to obtain the field components ( $B_x, B_y, B_z$ ) in the Hinode/SP field of view to give corresponding component uncertainties ( $\sigma_{B_x}, \sigma_{B_y}, \sigma_{B_z}$ ) (Leka & Skumanich 1999).

As with the De Rosa et al. (2009) approach, co-aligned MDI line-of-sight data are used initially to produce a potential field with a very large field of view, including AR 10954 roughly  $15^\circ$  to the east of AR 10953. However, the data-merging procedure deviates henceforth. The two datasets are re-sampled onto a  $0.5''$  grid (as compared to the original  $0.32''$  and  $1.8''$  resolution of the Hinode and MDI data, respectively). The computed MDI-derived image-plane potential vector field is merged with the coaligned Hinode/SP image-plane vector field (each component separately), by including a Hanning-function weighting at the boundary between the two datasets. This approach ensures a smooth transition between the data over a few pixels and avoids introducing spurious vertical currents due to sharp gradients between the two datasets.

The resulting combined Hinode/MDI vector field data and the uncertainties for each component are cropped to a field of view similar in size to that used by De Rosa et al. (2009) and Wheatland & Régnier (2009), and are re-sampled to the same  $0.8''$  resolution used in the previous investigations, resulting in a final  $313 \times 313$  grid. The  $B_z$  values used here are flux balanced to within 1%.

Values of  $\alpha_0$  are calculated for all points with  $|B_z| > 0.01 \times \max(B_z)$  using Equa-

tion (3), with centered differencing used to approximate the derivatives. Uncertainties  $\sigma_0$  for the force-free parameter boundary values are calculated at each point from  $(B_x, B_y, B_z)$  and  $(\sigma_{B_x}, \sigma_{B_y}, \sigma_{B_z})$  using propagation of errors applied to the differencing scheme (Leka & Skumanich 1999). A nominal large uncertainty value, equal to the maximum over all points, is assigned to points in the MDI field region. Points where the calculated  $\alpha_0$  is zero because  $|B_z| \leq 0.01 \times \max(B_z)$  are also assigned this nominal large uncertainty. The effect of this is that poorly-determined boundary values of  $\alpha$  carry little weight in the decisions on new boundary values made by the self-consistency procedure using Equation (4).

Figure 3 illustrates the resulting vector magnetogram for NOAA AR 10953. Panel (a) shows the values of  $B_z$ , and panel (b) shows the boundary values of  $J_z$ . The same color table (red-white-blue for negative-zero-positive values) used in Figure 2 is adopted. Panel (b) may be compared with Figure 3 in De Rosa et al. (2009) and Figure 3 in Wheatland & Régnier (2009), which show the current density values for the vector magnetogram used in the earlier studies. The current structures in the two sets of boundary data are very similar, including strong regions of current in the leading negative polarity spot, and less concentrated current structures in the more diffuse region of positive polarity. The new current map lacks the artifacts associated with the edge of the Hinode data region visible in the earlier data.

Figure 4 illustrates the quantitative values of the uncertainty estimates for  $B_z$  and  $J_z$  obtained for the vector magnetogram. This figure displays non-parametric estimates (e.g. Silverman 1986) of the density distribution of boundary points over values of  $|B_z|$  and  $\sigma_{B_z}$  [panel (a)], and over values of  $|J_z|$  and  $\sigma_{J_z}$  [panel (b)]. The uncertainty values for  $B_z$  illustrated in the panel (a) of Figure 4 are relatively small overall because the Hinode/SP-derived uncertainties are based solely on  $\chi^2$  fitting values, and do not include estimates of detection levels or systematic errors which would increase the uncertainty. Hence the estimates presented here should be considered to be lower bounds. The horizontal band of low uncertainty values for  $B_z$  in panel (a) of the figure represents the uniform noise in the MDI-derived areas. Panel (b) of Figure 4 shows a substantial horizontal band of large values of  $|J_z|$  with relatively small uncertainties, representing significant currents in the boundary data, as well as a vertical band of small  $|J_z|$  values with large uncertainties, representing points where the current is poorly determined.

### 3.2. Results

The current-field iteration method (Wheatland 2007) is applied to the data, as outlined in section 2.3, for 10 self-consistency cycles with 30 Grad-Rubin iterations used at each cycle to construct  $P$  and  $N$  solutions. Each solution is calculated on a  $313 \times 313 \times 300$  grid. The

horizontal grid size matches the boundary data, and the vertical grid size is chosen to include all field lines which do not cross the sides of the computational volume.

The treatment of ‘missing information’ associated with the absence of boundary conditions at the sides and top of the computational volume is important for coronal magnetic field reconstruction. The Wheatland (2007) method addresses this problem by neglecting currents on field lines which cross these boundaries. At each iteration for each solution, points  $\mathbf{r} = (x, y, z)$  on the grid threaded by field lines which cross the sides or top boundaries have  $\alpha(\mathbf{r})$  set to zero. This includes points  $(x, y, 0)$  on the grid in the lower boundary, so this procedure modifies the boundary values of the force-free parameter during the Grad-Rubin iterations. For boundary points subject to this modification the corresponding uncertainty in the force-free parameter is set equal to the nominal large uncertainty value discussed in section 3.1. This choice minimizes the effect of the zero values during the construction [according to Equation (4)] of a new set of  $\alpha$  boundary values at the end of a self-consistency cycle. The choice of the vertical grid size mentioned above also reduces the effect of this modification of the boundary conditions.

The self-consistency procedure converges in less than ten cycles. Figure 5 shows the self-consistent  $P$  and  $N$  solutions [panels (a) and (b) respectively] obtained after 10 cycles, using the same presentation as for the Wheatland & Régnier (2009) solution shown in Figure 2. Once again the red-white-blue images in the background show the boundary values of  $B_z$ , and the blue and red curves are field lines originating in  $P$  and  $N$  polarities respectively. The sets of field lines shown in panels (a) and (b) agree closely, demonstrating the self-consistency achieved. Some specific differences are visible for field lines extending higher into the computational volume. Table 1 lists values of the vector field comparison metrics introduced by Schrijver et al. (2006) in the context of testing nonlinear force-free methods on known solutions. The more stringent of these checks, the mean vector error and the normalized vector error, are both about 2% for the  $N$  solution compared with the  $P$  solution, which are small values for these metrics in this context (Schrijver et al. 2006; Metcalf et al. 2008; Wiegmann & Inhester 2010). The energies of the  $P$  and  $N$  solutions shown in Figure 5 are  $E/E_0 \approx 1.0822$  and  $E/E_0 \approx 1.0819$ , which differ by less than 0.03%. The two fields are sufficiently similar that we refer to the result as representing a single self-consistent solution.

The solution shown in Figure 5 is considerably more distorted from the potential configuration than the Wheatland & Régnier (2009) solution shown in Figure 2, consistent with the larger magnetic free energy (as discussed in section 2.4, the earlier solution has energy  $E/E_0 \approx 1.02$ ). The energy of the self-consistent solution obtained here ( $E/E_0 \approx 1.08$ ) is in the middle of the range of values reported in De Rosa et al. (2009) for different nonlinear force-free methods applied to preprocessed boundary data (the values were in the range

$E/E_0 \approx 1.03$ – $1.25$ ). The energy of the self-consistent solution obtained here is larger than the energy  $E/E_0 \approx 1.03$  of the  $P$  solution constructed at the first cycle from the vector magnetogram boundary values, but is smaller than the energy  $E/E_0 \approx 1.17$  of the  $N$  solution constructed initially. The averaging of  $\alpha$  values between foot points of field lines has led to a solution with an intermediate energy. The potential field has an energy  $E_0 \approx 8.40 \times 10^{32}$  erg, so the magnetic free energy for the region is about  $7 \times 10^{31}$  erg.

Figure 6 illustrates the convergence of the self-consistency procedure, showing the energies of the  $P$  and  $N$  solutions obtained at the end of each self-consistency cycle, versus cycle number. The  $P$ -solution energies are indicated by plus signs, and the  $N$ -solution energies by diamonds. The energy of the first  $N$  solution is substantially larger than the energy of the first  $P$  solution, as mentioned above. The solutions constructed at intermediate cycles approach one another in energy, converging in about eight cycles. During the initial self-consistency cycles, the Grad-Rubin iterations exhibit oscillation, as discussed in section 2.2. The boundary data contains large values of the electric current density which prevent strict convergence of the Grad-Rubin method. This introduces some arbitrariness into the modeling, because the exact  $P$  and  $N$  solutions, and hence the energies shown in Figure 6 depend on the choice of a stopping iteration. This problem is discussed in more detail below. The Grad-Rubin solutions constructed for later cycles converge quite strictly (a fixed point of the iteration scheme is achieved).

The self-consistency procedure changes the boundary values of the vertical electric current density and hence the boundary values of the horizontal field  $\mathbf{B}_h = (B_x, B_y)$ , but does not change the boundary values of  $B_z$ . Figure 7 illustrates the changes in the vertical current density  $J_z$  over the  $P$  and  $N$  polarities in the boundary. The self-consistency procedure reduces the largest values of  $|J_z|$  over both polarities, but retains some large currents. Many of the structures in the distribution of  $J_z$  observed in the initial data have survived, and in particular the patterns of strong-current in the leading negative polarity spot are preserved [see panels (c) and (d) of Figure 7], although the current distribution has changed in detail. Figure 8 illustrates the corresponding boundary values of the magnitude of the horizontal field at the photosphere, for the initial vector magnetogram and for the final self-consistent solution. Panel (a) of Figure 8 shows the horizontal field for the magnetogram data,  $B_h^i = \left[ (B_x^i)^2 + (B_y^i)^2 \right]^{1/2}$ , and panel (b) shows the the horizontal field for the self-consistent solution,  $B_h^f = \left[ (B_x^f)^2 + (B_y^f)^2 \right]^{1/2}$ . The maximum value of the two fields is very similar, and there is a good qualitative correspondence between features in the two images, although the details have changed.

Figure 9 illustrates the quantitative changes in the horizontal vector field, showing a

non-parametric estimate of the density of points (cf. Figure 4) over values of  $\Delta B_h/\sigma_{B_h}$  as a function of the measured  $B_h$ , where  $\Delta B_h = [(B_x^f - B_x^i)^2 + (B_y^f - B_y^i)^2]^{1/2}$  and  $\sigma_{B_h}$  is the uncertainty in  $B_h^i$ . Only points in the Hinode data region are included in this comparison. This figure indicates that the vast majority of points undergo small changes, but there is a substantial low-density tail of points subject to larger changes. The average absolute change in the horizontal field is  $\langle \Delta B_h \rangle \approx 170 \text{ Mx/cm}^2$ , and the average ratio of the changes to the uncertainties is  $\langle \Delta B_h/\sigma_{B_h} \rangle \approx 9$ . Many points are subject to changes in the horizontal field substantially larger than the corresponding uncertainty. As discussed in section 3.1, the uncertainties assigned to the vector magnetogram data are lower bounds. Also, the initial boundary data are physically inconsistent with the force-free model (the departure from the model is not due only to observational uncertainties). The absolute changes in the horizontal field are comparable to those produced by preprocessing (De Rosa et al. 2009).

A measure of the inconsistency between the boundary data and the force-free model is given by the estimates of the net forces and torques on the field in  $z > 0$  which may be calculated from the boundary data (Molodenskii 1969; Aly 1984, 1989), as discussed in section 2.2. Table 2 presents the values of the forces and torques for the initial vector magnetogram data, and for the self-consistent  $P$  and  $N$  solutions. The components of the initial force are of order a few percent, and the components of the initial torque are of order 10%, in terms of relevant characteristic values. For the self-consistent solutions the force components are reduced to  $< 0.1\%$ , and the components of the torques are reduced to  $\lesssim 0.1\%$  (in most cases much less), with the same scaling. The changes in the horizontal field and hence current illustrated in Figures 7–9 are necessary to achieve this consistency with the force-free model.

As mentioned above, the Grad-Rubin iterations do not converge exactly during the early and intermediate self-consistency cycles, and the choice of the final iteration for each cycle introduces some arbitrariness into the procedure. To investigate this effect the calculation is repeated, with  $N_{\text{GR}} = 20$  Grad-Rubin iterations per cycle for both the  $P$  and  $N$  solutions (rather than  $N_{\text{GR}} = 30$ ), also with  $N_{\text{GR}} = 40$  iterations per cycle. The Grad-Rubin iterations converge in  $\lesssim 20$  cycles for later cycles, so  $N_{\text{GR}} = 20$  is approximately the minimum suitable choice. In each case, the self-consistency procedure is found to converge in less than 10 cycles. The self-consistent fields obtained with  $N_{\text{GR}} = 20$  and  $N_{\text{GR}} = 40$  are qualitative very similar to the  $N_{\text{GR}} = 30$  result, i.e. the field lines are visually very similar. The energies are also remarkably similar, with all three solutions having  $E/E_0 \approx 1.08$ , to the stated digits. Table 3 quotes the vector field comparison metrics from Schrijver et al. (2006), comparing the  $P$  solutions of the two new cases ( $N_{\text{GR}} = 20$  and  $N_{\text{GR}} = 40$ ) with the original case ( $N_{\text{GR}} = 30$ ). The values are substantially larger than for the comparison of the individual  $P$  and  $N$  solutions (e.g. Table 1), but are smaller than the typical differences introduced by

varying treatments of the unknown side and top boundary conditions in the application of nonlinear force-free methods to known solutions (Schrijver et al. 2006; Metcalf et al. 2008). Hence in the context of nonlinear force-free modeling, the solutions may be considered very similar.

Figure 10 illustrates the boundary distributions of  $J_z$  for the three self-consistent  $N$  solutions. Panel (a) shows the signal to noise ratio values  $\alpha_0/\sigma_0$  over the vector magnetogram, which determine how well the initial boundary conditions on  $J_z$  are preserved at different locations in the boundary by the self-consistency procedure, according to the first of Equations (4). Panels (b), (c), and (d) show the boundary conditions on  $J_z$  in the self-consistent solutions for the cases  $N_{\text{GR}} = 20$ ,  $N_{\text{GR}} = 30$ , and  $N_{\text{GR}} = 40$  respectively, using the same presentation as Figures 3 and 7. Panels (b)–(d) are visually very similar. The same structures are observed, and the range of values of  $J_z$  is very similar. Comparison with the signal to noise ratio map [panel (a)] illustrates qualitatively how the current is unchanged at locations where  $\alpha_0$  (or  $J_z$ ) is well-determined. These results suggest that the self-consistency procedure, including uncertainties, is identifying a particular force-free solution independent of this element of arbitrariness.

#### 4. Discussion

A solution to the nonlinear force-free model is constructed for NOAA solar active region AR 10953, based on a vector magnetogram derived from Hinode/SOT observations at 22:30 UT on 30 April 2007. The solution applies the ‘self-consistency’ procedure of Wheatland & Régnier (2009), for the first time taking into account uncertainties in the boundary data. The boundary data are subject to improved techniques for data merging by comparison with earlier studies using the same Hinode/SOT observations (De Rosa et al. 2009; Wheatland & Régnier 2009). The self-consistency procedure addresses the problem that vector magnetogram data are inconsistent with the force-free model (De Rosa et al. 2009; Wheatland et al. 2010). In particular, the solar boundary data provide two possible force-free solutions (the  $P$  and  $N$  solutions, corresponding to choosing boundary conditions for the vertical electric current density  $J_z$  from the positive or the negative polarities of the boundary field respectively), which are generally found to be significantly different. The  $P$  and the  $N$  solutions are distinctly different for the vector magnetogram data used here. The self-consistency procedure modifies the boundary conditions on  $J_z$  during a sequence of cycles in which  $P$  and  $N$  solutions are constructed using Grad-Rubin iteration (Wheatland 2007), and arrives at a solution to the force-free model with boundary values close to, but not exactly matching, the observational vector magnetogram data. When uncertainties in

the boundary data are taken into account, the boundary values of  $J_z$  are preserved more closely at points having smaller uncertainties.

Self-consistency modeling has two advantages over conventional force-free modeling. First, force-free methods tend to fail to strictly converge when applied to solar data, and hence do not accurately solve the force-free model. The self-consistency procedure achieves strict convergence. Second, the method identifies a single solution, rather than two solutions. Active region AR 10953 was previously modelled using the self-consistency procedure in Wheatland & Régnier (2009), but in that case uncertainties were not included, and the results were regarded as a proof of concept of the method, rather than a full demonstration of its capabilities. This paper presents a more comprehensive demonstration and investigation.

The self-consistent solution obtained for active region AR 10953 is substantially non-potential, with a coronal magnetic energy  $E/E_0 \approx 1.08$ , where  $E_0$  is the energy of the potential field with the same vertical component of the magnetic field in the boundary. This energy is significantly larger than the energy  $E/E_0 \approx 1.02$  of the solution obtained in Wheatland & Régnier (2009), which is attributed to the neglect of uncertainties in the earlier paper. The non-potentiality of the region is due to strong currents in the inner parts of the region, in particular associated with the southern part of the the negative polarity leading spot, as shown in Figure 3. These currents were reduced in the earlier solution by the self-consistency averaging procedure [Equations (4)] due to the omission of uncertainties (or rather, the treatment of all boundary points as having equal uncertainty). With uncertainties included correctly, these currents are preserved because they are in regions where the field, and hence current, is well-determined, as shown in Figure 10.

The energy of the new self-consistent solution is intermediate between the energies of the  $P$  and  $N$  solutions constructed from the vector magnetogram data ( $E/E_0 \approx 1.03$  for the  $P$  solution, and  $E/E_0 \approx 1.17$  for the  $N$  solution), and is also in the middle of the range of energies found by De Rosa et al. (2009) using force-free codes applied to boundary data derived from the same Hinode/SOT observations but subject to the preprocessing procedure (Wiegelmann, Inhester, & Sakurai 2006; Wiegelmann et al. 2008), which is not used here. Recently Canou & Amari (2010) presented a more detailed account of force-free modeling of AR 10953 with two Grad-Rubin codes applied to the  $N$ -polarity De Rosa et al. (2009) boundary data, and reported energies  $E/E_0 \approx 1.27$  and  $E/E_0 \approx 1.31$ . The energies obtained by these authors are different from the energy of the initial  $N$  solution obtained here for a number of reasons. The Hinode/MDI boundary data used here is prepared differently, as discussed in section 3.1, and preprocessing has not been applied. The lack of convergence of the initial  $P$  and  $N$  solutions obtained here means that a range of energies is possible, depending on the choice of stopping iteration (in practise we find energies for the  $N$  solution



in the range  $E/E_0 \approx 1.16$  to  $E/E_0 \approx 1.22$ ). The present method treats the side and top boundaries in a different way to the Canou & Amari (2010) method, and in particular we neglect currents on field lines which cross the side and top boundaries, which tends to reduce the energy. Finally, the stated Canou & Amari (2010) and De Rosa et al. (2009) energies refer to a smaller sub-region of the computational domain. Because of these differences we do not attempt a more detailed comparison with the earlier results.

A degree of arbitrariness is introduced into the modeling by the lack of strict convergence of the Grad-Rubin iterations used to construct the  $P$  and  $N$  solutions at early and intermediate self-consistency cycles. The results of the self-consistency procedure may depend on the choice of the number of Grad-Rubin iterations. This effect is investigated by repeating the calculation with  $N_{\text{GR}} = 20$  and  $N_{\text{GR}} = 40$  iterations at each cycle (rather than  $N_{\text{GR}} = 30$ ). The two new self-consistent solutions are remarkably similar to the first solution, and in particular all three solutions have energy  $E/E_0 \approx 1.08$ . This suggests that self-consistency modeling provides a solution to the problem of reliable estimation of the coronal magnetic free energy of an active region, once uncertainties in the boundary data are incorporated. The inclusion of uncertainties preserves boundary conditions on current at points in the boundary where the currents are most accurately determined. The three self-consistent solutions obtained with different numbers of Grad-Rubin iterations have very similar boundary distributions of  $J_z$ .

The self-consistency procedure (including uncertainties) is a promising candidate for routine reconstruction of coronal magnetic fields. The technique is shown to produce a highly non-potential and accurately force-free coronal field model for NOAA AR 10953 from Hinode/SOT vector magnetogram data. The estimate of the free energy of the magnetic field appears to be robust based on the results obtained with varying numbers of Grad-Rubin iterations per self-consistency cycle. The availability of high-quality vector magnetogram data over the next solar cycle from Hinode/SOT and SDO/HMI will provide ample opportunities for further testing, development, and application of the method, to investigate many questions in the physics of solar activity.

Hinode is a Japanese mission developed and launched by ISAS/JAXA, collaborating with NAOJ as a domestic partner, and NASA and STFC (UK) as international partners. Scientific operation of the Hinode mission is conducted by the Hinode science team organized at ISAS/JAXA. This team mainly consists of scientists from institutes in the partner countries. Support for the post-launch operation is provided by JAXA and NAOJ (Japan), STFC (U.K.), NASA, ESA, and NSC (Norway). We extend our thanks to Bruce Lites for providing the full inversion results for the data used herein and Paul Seagraves for developing the code at NCAR/HAO. KDL appreciates funding from NSF SHINE grant ATM-0454610

and NPDE code from Graham Barnes. Mike Wheatland acknowledges support from the same NSF SHINE grant during a collaborative visit to NWRA in Boulder.

*Facilities:* Hinode, SOHO.

## REFERENCES

- Aly, J. J. 1984, ApJ, 283, 349
- Aly, J. J. 1989, Sol. Phys., 120, 19
- Aly, J. J., & Amari, T. 2007, Geophys. Astrophys. Fluid Dyn., 101, 249
- Auer, L. H., House, L. L., & Heasley, J. N. 1977, Sol. Phys., 55, 47
- Amari, T., Aly, J. J., Luciani, J. F., Boulmezaoud, T. Z., & Mikic, Z. 1997, Sol. Phys., 174, 129
- Amari, T., Boulmezaoud, T. Z., & Aly, J. J. 2006, A&A, 446, 691
- Bommier, V., Landi Degl’Innocenti, E., Landolfi, M., & Molodij, G. 2007, A&A, 464, 323
- Borrero, J. M., Tomczyk, S., Norton, A., Darnell, T., Schou, J., Scherrer, P., Bush, R., & Liu, Y. 2007, Sol. Phys., 240, 177
- Canou, A., & Amari, T. 2010, ApJ, 715, 1566
- Committee On The Societal, and Economic Impacts Of Severe Space Weather Events 2008, Severe Space Weather Events: Understanding Societal and Economic Impacts Workshop Report, Space Studies Board ad hoc Committee on the Societal & Economic Impacts of Severe Space Weather Events: A Workshop, The National Academies Press: Washington, DC ISBN: 978-0-309-12769-1
- Del Toro Iniesta, J. C., & Ruiz Cobo, B. 1996, Sol. Phys., 164, 169
- De Rosa, M. L., et al. 2009, ApJ, 696, 1780
- Gary, G. A. 2001, Sol. Phys., 203, 71
- Grad, H. and Rubin, H. 1958, in Proc. 2nd Int. Conf. on Peaceful Uses of Atomic Energy, Vol. 31, Geneva: UN, 190
- Inhester, B., & Wiegmann, T. 2006, Sol. Phys., 235, 201

- Jaynes, E. T. 2003, *Probability Theory*, by E. T. Jaynes, ed. G. Larry Bretthorst, Cambridge, UK: Cambridge University Press
- Landi Degl’Innocenti, E. & Landolfi, M. 2004, *Polarization in Spectral Lines*, Kluwer: Dordrecht
- Landolfi, M., & Landi Degl’Innocenti, E. 1982, *Sol. Phys.*78, 355
- Leka, K. D., Barnes, G., Crouch, A. D., Metcalf, T. R., Gary, G. A., Jing, J., & Liu, Y. 2009, *Sol. Phys.*260, 83
- Leka, K. D., & Skumanich, A. 1999, *Sol. Phys.*, 188, 3
- Leka, K. D. 1999, *Sol. Phys.*, 188, 21
- Lites, B.W. 2009, private communication
- McClymont, A. N., Jiao, L., & Mikic, Z. 1997, *Sol. Phys.*, 174, 191
- Metcalf, T. R. 1994, *Sol. Phys.*, 155, 235
- Metcalf, T. R., Jiao, L., McClymont, A. N., Canfield, R. C., & Uitenbroek, H. 1995, *ApJ*, 439, 474
- Metcalf, T. R., et al. 2006, *Sol. Phys.*, 237, 267
- Metcalf, T. R., et al. 2008, *Sol. Phys.*, 247, 269
- Molodenskii, M. M. 1969, *Soviet Ast.*, 12, 585
- Neukirch, T. 2005, in Innes, D.E., Lagg, A., Solanki, S.K. (eds.), *Proceedings of the International Scientific Conference on Chromospheric and Coronal Magnetic Fields*, ESA SP-596, 12.1 (CDROM)
- Odenwald, S., Green, J., & Taylor, W. 2006, *Adv. Space Res.* 38, 280
- Régnier, S. 2007, *Mem. Soc. Astron. Italiana*, 78, 126
- Sakurai, T. 1981, *Sol. Phys.*, 69, 343
- Scherrer, P. H., et al. 1995, *Sol. Phys.*, 162, 129
- Scherrer, P.H., Hoeksema, J.T., & the HMI Team 2006, 36th COSPAR Scientific Assembly, 36, 1469.

- Schrijver, C. J., et al. 2006, *Sol. Phys.*, 235, 161
- Schrijver, C. J., et al. 2008, *ApJ*, 675, 1637
- Silverman, B. W. 1986, *Density Estimation for Statistics and Data Analysis*, Chapman & Hall: Boca Raton
- Skumanich, A., & Lites, B. W. 1987, *ApJ*, 322, 473
- Sturrock, P. A. 1994, *Plasma Physics*, Cambridge University Press: Cambridge
- Tsuneta, S., et al. 2008, *Sol. Phys.*, 249, 167
- Wheatland, M. S., Sturrock, P. A., & Roumeliotis, G. 2000, *ApJ*, 540, 1150
- Wheatland, M. S. 2007, *Sol. Phys.*, 245, 251
- Wheatland, M. S., & Régnier, S. 2009, *ApJ*, 700, L88
- Wheatland, M. S., Gilchrist, S.A., & Régnier, S. 2010, *Advances in Geosciences (A 6-Volume Set)*, Volume 21: Solar Terrestrial (ST), Vol. 21 Editor-in-Chief Marc Duldig, World Scientific: Singapore
- Wiegelmann, T. 2004, *Sol. Phys.*, 219, 87
- Wiegelmann, T., & Inhester, B. 2010, *A&A*, 516, A107
- Wiegelmann, T., Inhester, B., & Sakurai, T. 2006, *Sol. Phys.*, 233, 215
- Wiegelmann, T. 2008, *J. Geophys. Res.(Space Physics)*, 113, 3
- Wiegelmann, T., Thalmann, J. K., Schrijver, C. J., De Rosa, M. L., & Metcalf, T. R. 2008, *Sol. Phys.*, 247, 249

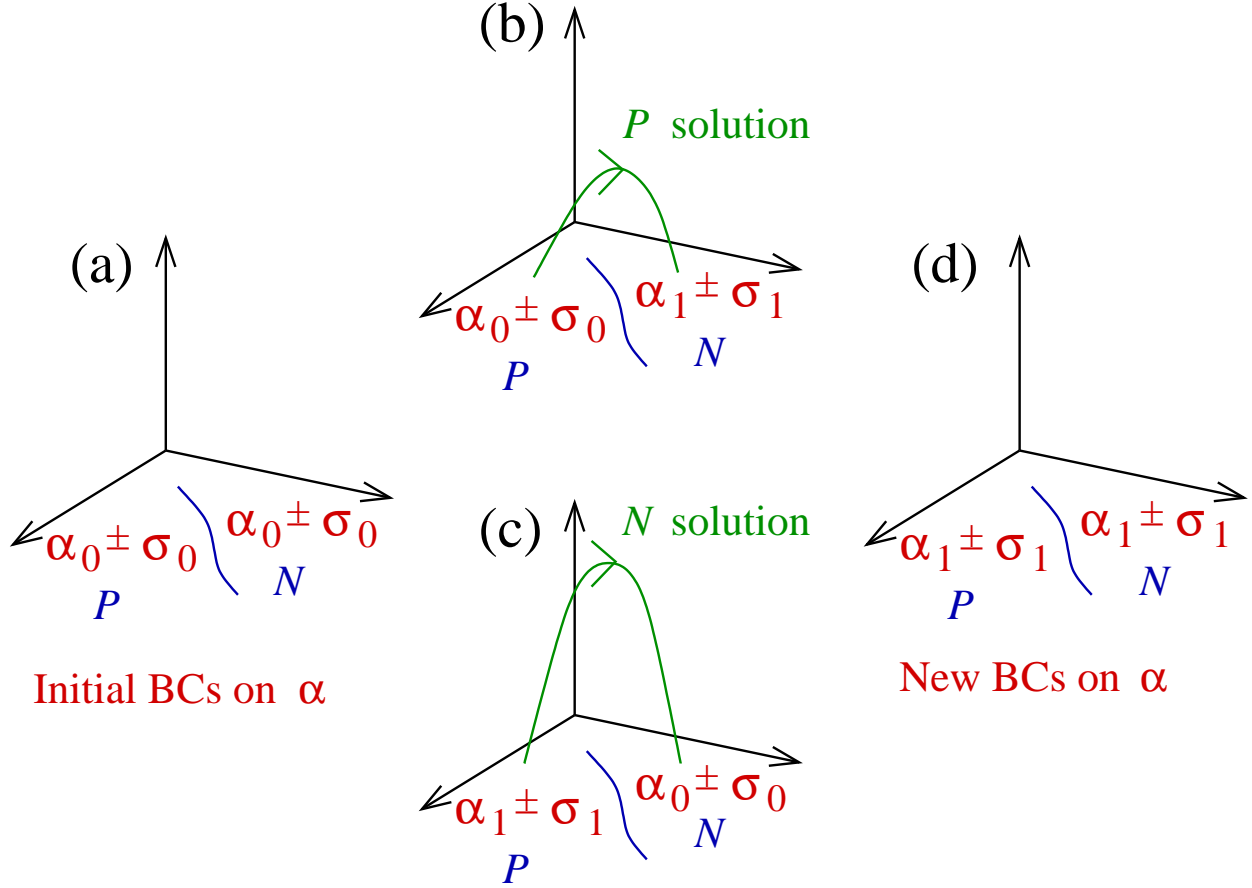


Fig. 1.— The first step of the self-consistency procedure. Two solutions are constructed from the  $P$  (positive polarity) and  $N$  (negative polarity) boundary values of the force-free parameter  $\alpha_0$ , shown in panel (a). The  $P$  and  $N$  solutions map values of  $\alpha_0 \pm \sigma_0$  along magnetic field lines from  $P \rightarrow N$  and from  $N \rightarrow P$  respectively, as illustrated in panels (b) and (c) respectively. These mappings define a new set of boundary conditions ( $\alpha_1 \pm \sigma_1$ ) over  $P$  and  $N$ , as shown in panel (d). The blue curves in the boundary in each panel indicate the neutral line dividing  $P$  and  $N$ , and the green curves in panels (b) and (c) are field lines of the  $P$  and  $N$  solutions, with arrows indicating field direction.

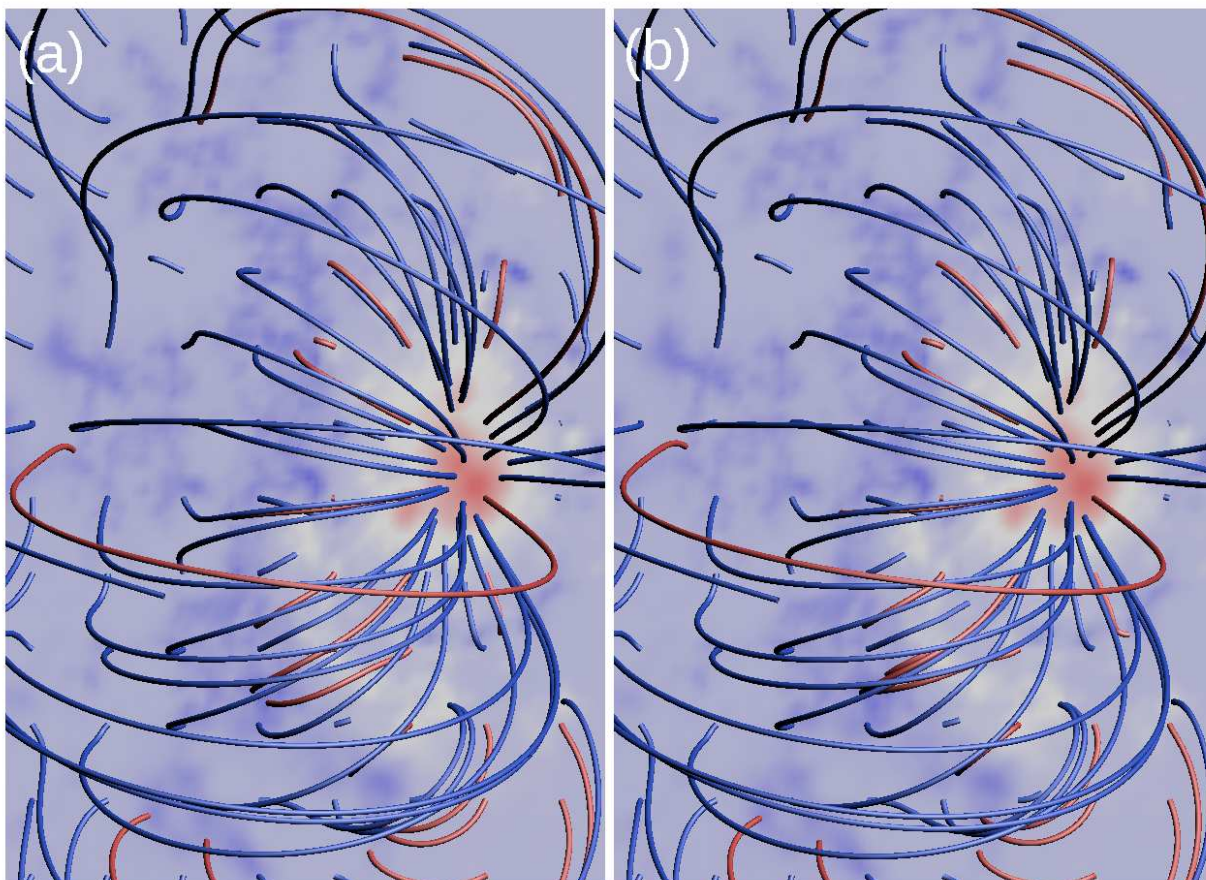


Fig. 2.— The self-consistent solution for the coronal magnetic field of NOAA AR 10953 obtained by Wheatland & Régnier (2009). Panel (a) shows the  $P$  solution and panel (b) shows the  $N$  solution, after 10 self-consistency cycles. The color image in the background in each case shows the boundary values of  $B_z$ , with negative values red, values close to zero white, and positive values blue. The blue curves in each panel are field lines originating at points in the  $P$  polarity, and the red curves are field lines originating at points in the  $N$  polarity. The sets of field lines for the  $P$  solution in panel (a) and for the  $N$  solution in panel (b) agree closely.

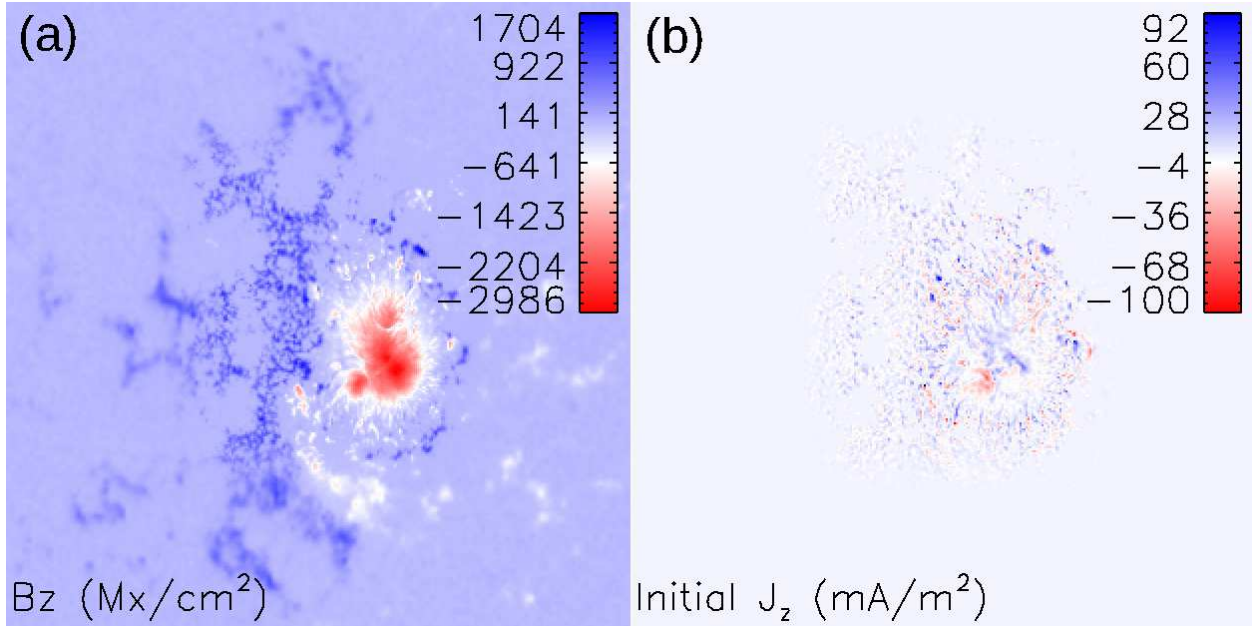


Fig. 3.— The vector magnetogram boundary data for NOAA AR 10953 used in the magnetic field reconstructions in this paper. Panel (a): photospheric values of the vertical field  $B_z$ . Panel (b): initial photospheric values of the vertical electric current density  $J_z$ .

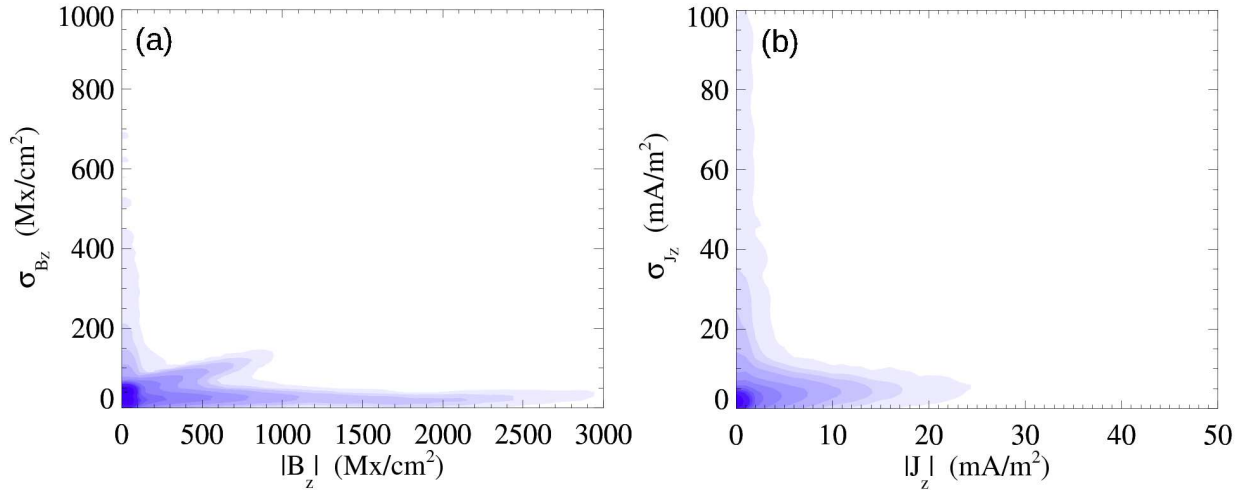


Fig. 4.— The uncertainties in the vector magnetogram boundary values of the field, represented using non-parametric estimates of the density distributions of boundary points. Panel (a): density distribution over values of  $|B_z|$  and  $\sigma_{B_z}$ . Panel (b): density distribution over  $|J_z|$  and  $\sigma_{J_z}$ .

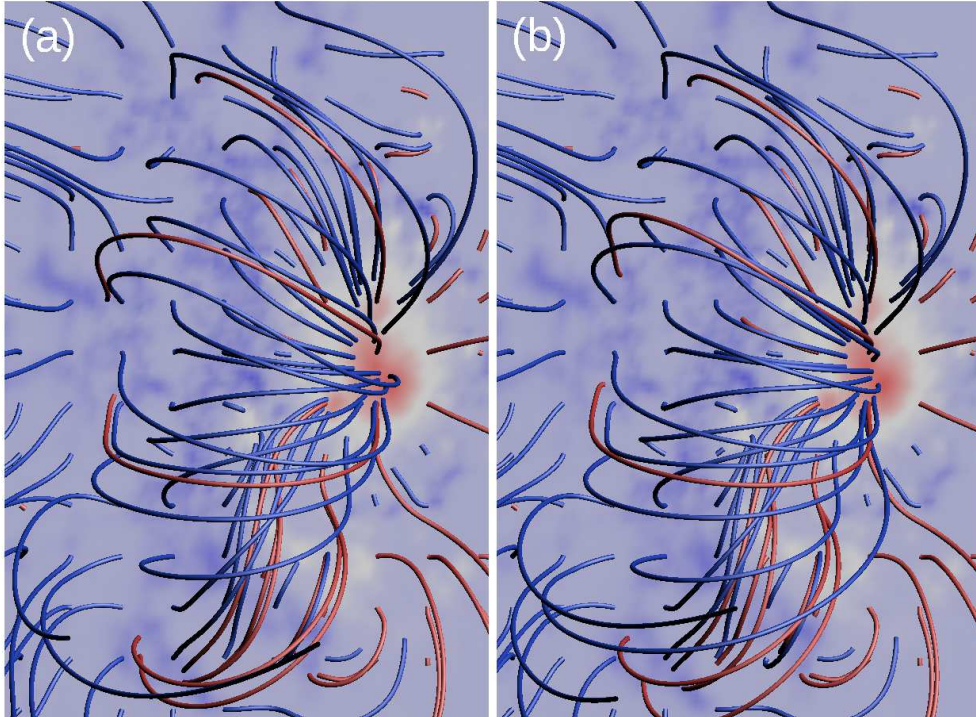


Fig. 5.— The self-consistent solution for the coronal magnetic field of NOAA AR 10953 obtained using the new vector magnetogram boundary data including uncertainties. The presentation is the same as for Figure 2. Panel (a) shows the  $P$  solution and panel (b) shows the  $N$  solution, after 10 self-consistency cycles. The color images in the background are the boundary values of  $B_z$ , and the blue/red curves are field lines originating in the  $P/N$  polarities. The sets of field lines for the  $P$  solution in panel (a) and for the  $N$  solution in panel (b) agree closely.



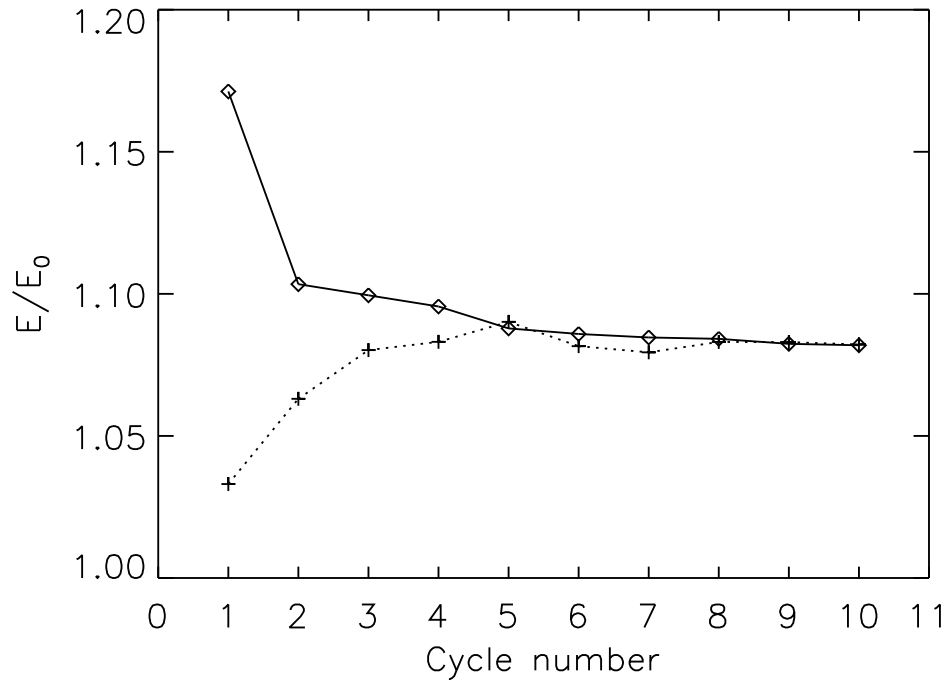


Fig. 6.— The energy of the  $P$  solutions (plus signs) and the  $N$  solutions (diamonds) constructed at each self-consistency cycle, in units of the reference potential field energy.

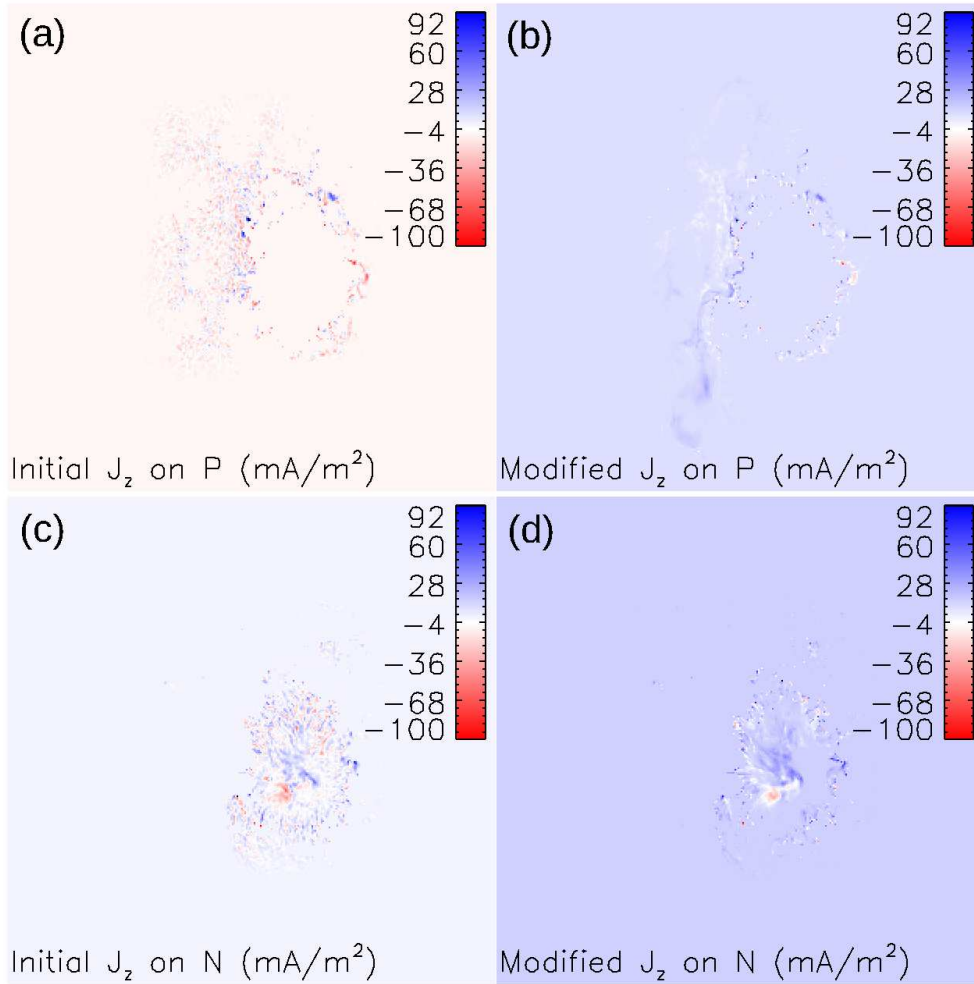


Fig. 7.— Initial boundary conditions on  $J_z$  and the boundary conditions on  $J_z$  for the self-consistent solution, for each polarity. Panel (a) shows the initial  $J_z$  values over  $P$ , and panel (b) shows the self-consistent  $J_z$  values over  $P$ . Panels (c) and (d) show the same quantities, respectively, over  $N$ .

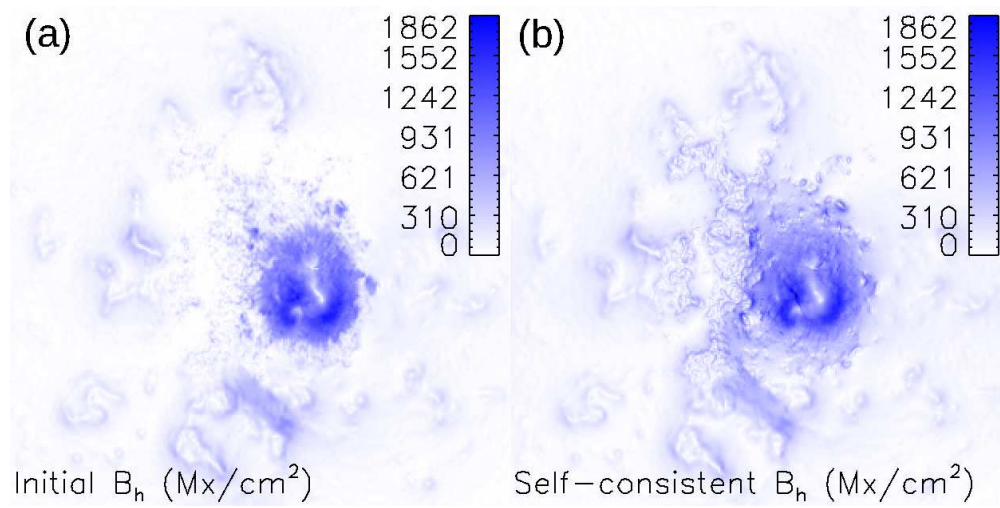


Fig. 8.— Panel (a): The horizontal field at the photosphere for the vector magnetogram. Panel (b): the horizontal field at the photosphere for the self-consistent solution.

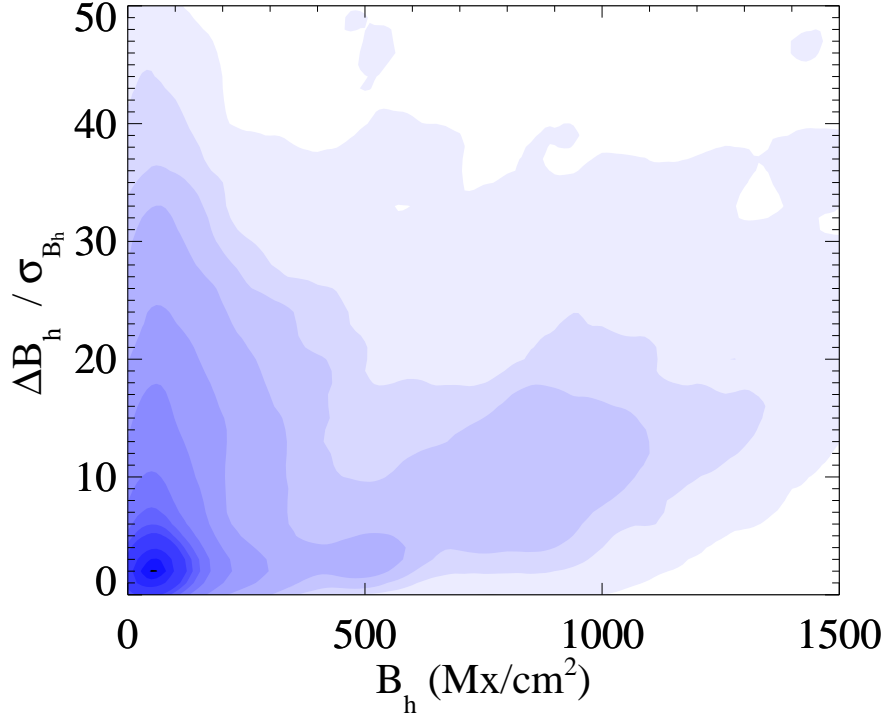


Fig. 9.— Quantitative changes in the horizontal field at the photosphere produced by the self-consistency procedure. A non-parametric estimate of the density distribution of boundary points, showing  $\Delta B_h / \sigma_{B_h}$  as a function of the initial  $B_h$  magnitude, where  $\sigma_{B_h}$  is the uncertainty in the magnitude of the initial horizontal field, and  $\Delta B_h = [(B_x^f - B_x^i)^2 + (B_y^f - B_y^i)^2]^{1/2}$  is the change in the horizontal field, with  $i$  denoting values in the initial vector magnetogram, and  $f$  the final values in the self-consistent solution.

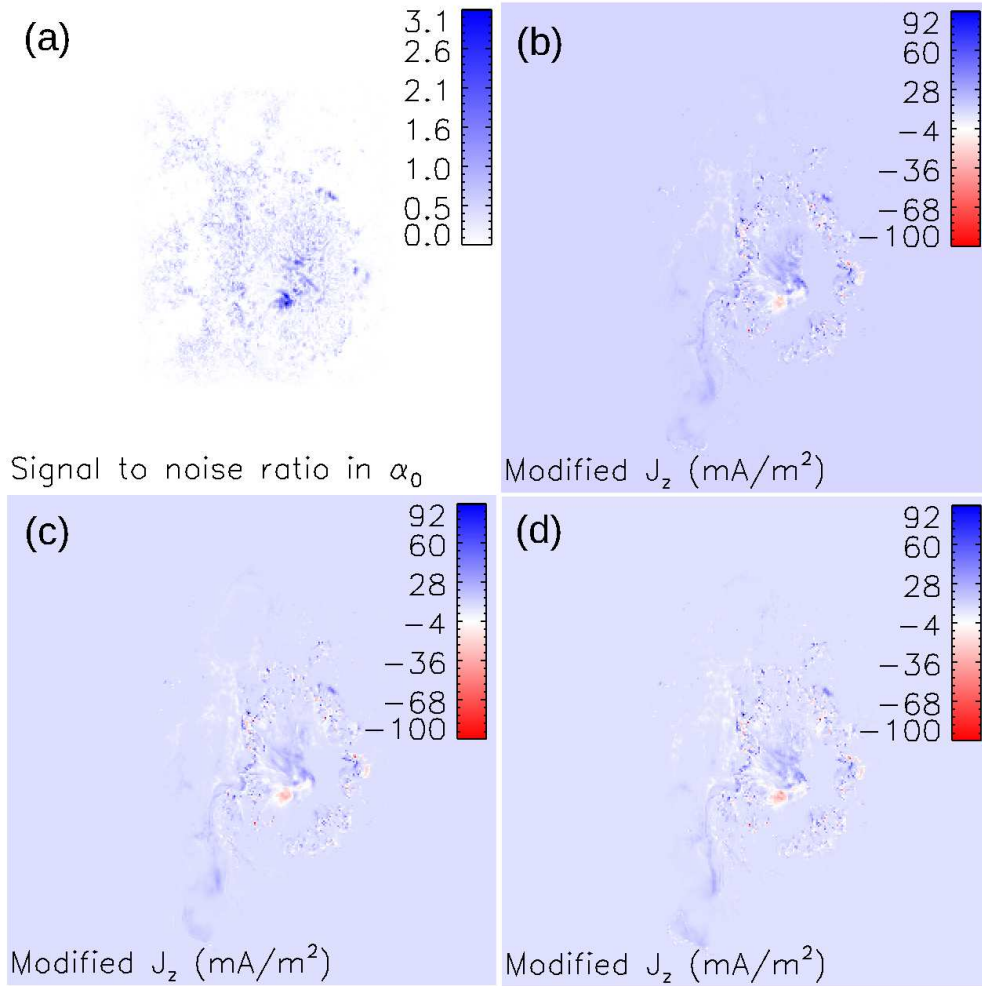


Fig. 10.— Panel (a) shows a map of the signal to noise ratio for  $\alpha_0$ , which determines how well the initial boundary conditions on  $J_z$  are preserved by the self-consistency procedure. Panels (b), (c), and (d) show the boundary conditions on  $J_z$  for the self-consistent  $N$  solutions obtained using 20, 30, and 40 Grad-Rubin iterations per self-consistency cycle respectively.

Table 1: Vector field comparison metrics for the calculated self-consistent  $P$  and  $N$  solution fields, for the default calculation (with 30 Grad-Rubin iterations per self-consistency cycle).

Metric <sup>a</sup>	Value
1 – CS	$8 \times 10^{-6}$
1 – VC	$3 \times 10^{-4}$
MVE	$2 \times 10^{-2}$
NVE	$2 \times 10^{-2}$

<sup>a</sup>These metrics were introduced by Schrijver et al. (2006). CS is the Cauchy-Schwarz metric,  $CS = M^{-1} \sum_i \mathbf{B}_{1i} \cdot \mathbf{B}_{2i} / (B_{1i} B_{2i})$ , where  $\mathbf{B}_1$  is the  $P$  solution and  $\mathbf{B}_2$  is the  $N$  solution, the sum is over all grid points enumerated by  $i$ , and  $M = 313 \times 313 \times 300$  is the total number of grid points. VC is the vector correlation,  $VC = \sum_i \mathbf{B}_{1i} \cdot \mathbf{B}_{2i} / \sqrt{\sum_i B_{1i}^2 \sum_i B_{2i}^2}$ . MVE is the mean vector error,  $MVE = M^{-1} \sum_i |\mathbf{B}_{1i} - \mathbf{B}_{2i}| / B_{1i}$ , and NVE is the normalized vector error,  $NVE = \sum_i |\mathbf{B}_{1i} - \mathbf{B}_{2i}| / \sum_i B_{1i}$ .

Table 2: Estimates of the components of the net force  $\mathbf{F}$  and net torque  $\mathbf{\Gamma}$  on the coronal volume above NOAA AR 10953.

Quantity	Vector magnetogram	Self-consistent P solution	Self-consistent N solution
$F_x/F_0^a$	$-1.2 \times 10^{-2}$	$4.8 \times 10^{-4}$	$4.3 \times 10^{-4}$
$F_y/F_0$	$3.9 \times 10^{-2}$	$7.1 \times 10^{-4}$	$6.5 \times 10^{-4}$
$F_z/F_0$	$-7.0 \times 10^{-2}$	$-5.1 \times 10^{-5}$	$7.1 \times 10^{-4}$
$\Gamma_x/\Gamma_0^b$	$-1.2 \times 10^{-1}$	$1.1 \times 10^{-3}$	$1.9 \times 10^{-4}$
$\Gamma_y/\Gamma_0$	$1.2 \times 10^{-1}$	$-2.5 \times 10^{-4}$	$1.9 \times 10^{-4}$
$\Gamma_z/\Gamma_0$	$3.9 \times 10^{-2}$	$-7.6 \times 10^{-5}$	$-1.0 \times 10^{-4}$

<sup>a</sup>The forces are in units of  $F_0 = \int p_B dx dy$  with  $p_B = (B_x^2 + B_y^2 + B_z^2)/2\mu_0$ , where the integral is performed over the magnetogram area with the origin for the coordinates at the lower left corner.

<sup>b</sup>The torques are in units of  $\Gamma_0 = \int x p_B dx dy$ , with  $p_B = (B_x^2 + B_y^2 + B_z^2)/2\mu_0$ , where the integral is performed over the magnetogram area with the origin for the coordinates at the lower left corner.

Table 3: Vector field comparison metrics for the self-consistent  $P$  solutions calculated with different numbers of Grad-Rubin iterations per self-consistency cycle. The comparisons are for the solutions with  $N_{\text{GR}} = 20$  and  $N_{\text{GR}} = 30$ , and for the solutions with  $N_{\text{GR}} = 20$  and  $N_{\text{GR}} = 30$ .

Metric <sup>a</sup>	$N_{\text{GR}} = 30$ and $N_{\text{GR}} = 20$	$N_{\text{GR}} = 30$ and $N_{\text{GR}} = 40$
1 – CS	$5 \times 10^{-4}$	$4 \times 10^{-4}$
1 – VC	$3 \times 10^{-3}$	$3 \times 10^{-3}$
MVE	0.08	0.09
NVE	0.08	0.09

---

<sup>a</sup>The definitions of the metrics are the same as given in Table 1, with  $\mathbf{B}_1$  representing the  $N_{\text{GR}} = 30$  solution and  $\mathbf{B}_2$  the solution with either  $N_{\text{GR}} = 20$  or  $N_{\text{GR}} = 30$ .